Guided wave tomography with an improved scattering model

P. Huthwaite

12th December 2016

Abstract

Producing accurate thickness maps of corrosion damage is of great importance for assessing life in the petrochemical industry. Guided wave tomography provides a solution for this, by sending guided waves through the region of interest, then using tomographic imaging techniques to reconstruct the thickness map, importantly eliminating the need to take measurements at all points across the surface. However, to achieve accurate maps, the imaging algorithm must account for the way in which the guided waves interact with corrosion defects, and the complex scattering which occurs. Traditional approaches have exploited the dispersive nature of guided waves: a velocity map is produced from a data set, then converted to thickness using the dispersion relationship. However, these relationships are derived for plates of constant thickness, which is not the case in the majority of defects, causing significant inaccuracies exist in the images. This paper develops a more sophisticated inversion solution which accounts for the full guided wave scattering. Through this, more accurate images with resolution better than a wavelength, compared to two wavelengths previously. This is demonstrated with simulated and experimental data. The speed and stability of the algorithm in the presence of random noise and systematic errors is also demonstrated.

Keywords

Guided waves, tomography, imaging, scattering

1 Introduction

Assessing the remaining life of assets is critical in the petrochemical industry, particularly in the presence of corrosion which reduces wall thickness of pipes and pressure vessels, increasing the chance of unexpected failure. Guided wave tomography [1] is a quantitative technique proposed to produce wall-thickness maps of pipes and plates; this enables the remaining thickness to be extracted and hence the life of the component to be determined, without requiring access to all points on the surface, making it a potentially valuable non-destructive testing technique. Lamb waves are excited in a plate or plate-like-structure (including pipe walls provided the wall is thin compared to the radius of curvature, meaning that curvature can be neglected [2]) from an array of transducers; these then interact with a region potentially containing wall thinning caused by corrosion, and the resulting waves are measured by another array. These measurements are subsequently processed to produce a thickness map.

Clearly, it is critical that these maps are an accurate representation of the true map to avoid the risks associated with overestimating remaining life, or waste associated with underestimating it. This accuracy is highly dependent on the underlying assumptions used in the reconstruction. The primary assumption used reformulates the guided wave scattering problem as one of acoustic waves being scattered by velocity [3]. As shown in the dispersion curves of Fig. 1, the guided wave velocity is a function of the frequency-thickness product, so by fixing frequency, wave velocity can be shown to be a function of thickness. This is a widely used assumption which has been utilised for 20 years in guided wave tomography [3–12] but relies on a key approximation. The dispersion curves are derived for infinite plates of constant thickness [13], and therefore it assumes that any local thickness variations are sufficiently gradual that they can be neglected. As highlighted in [14] this manifests itself as a resolution limit in the reconstruction of around 2λ, effectively applying a low-pass filter to remove any higher spatial frequency components. This limit corresponds to $8T$ where T is wall thickness at 0.5MHz-mm A0, or $4T$ at the constant group velocity around of 1.4MHz-mm A0. Importantly this limit is sufficient to cause significant inaccuracies with typical corrosion defects.

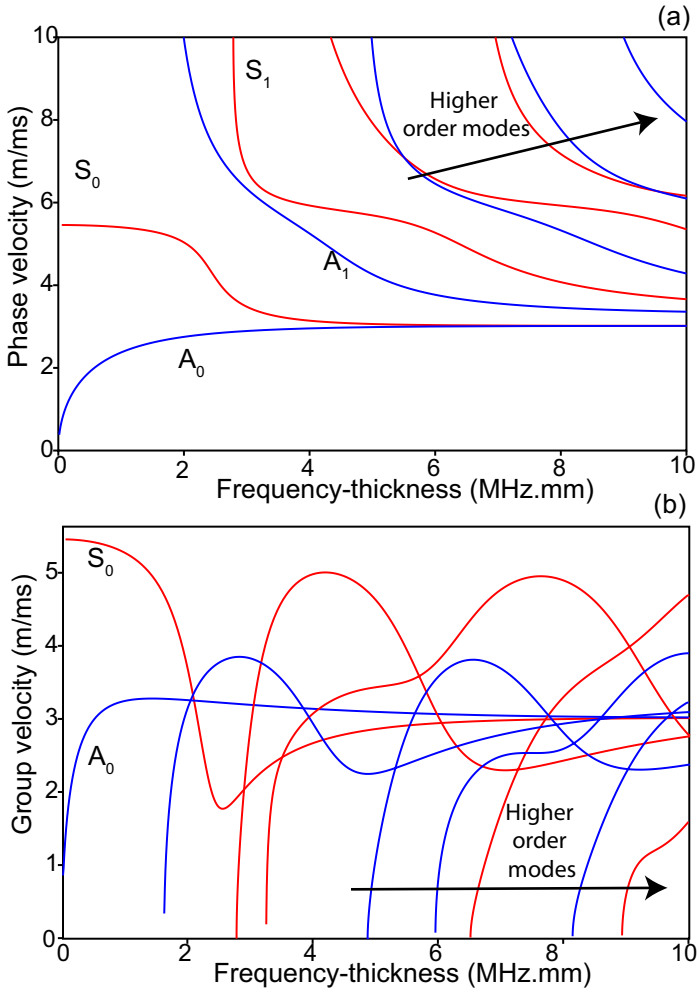

Figure 1: Dispersion curves for a steel plate. (a) presents phase velocity as a function of frequency-thickness for a number of modes. (b) presents the group velocity.

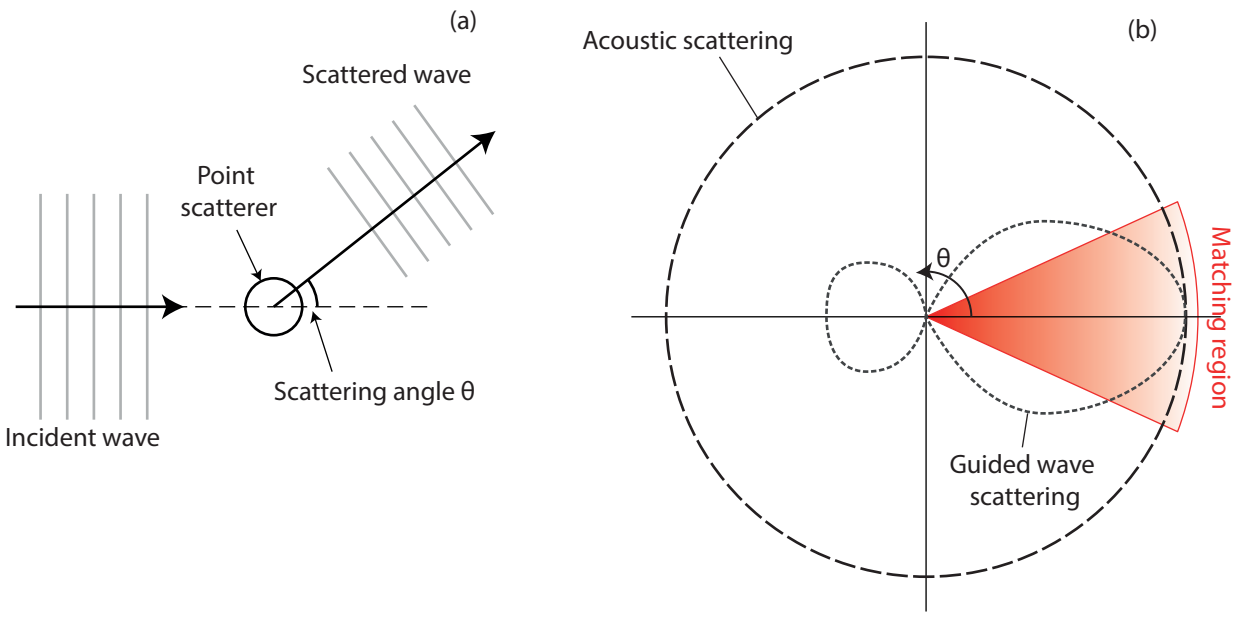

Figure 2: Schematic comparing acoustic and guided wave scattering behaviour. (a) shows the definition of the scattering angle θ for a point scatterer, and (b) then presents typical scattering patterns as a function of this scattering angle for acoustic and guided wave scattering from such a point scatterer. (b) also highlights a region in which reasonably good matching is seen between the guided wave and acoustic models.

This lack of resolution when compared to the traditional limit of $\lambda/2$ can also be considered to be an effect of the different scattering behaviour observed between guided waves with varying thickness and acoustic waves with varying velocity. Figure 2 presents a schematic of this. Fig. 2(a) defines the scattering angle, while Fig. 2(b) plots the scattering patterns for an acoustic and guided wave model. The acoustic case has a omnidirectional behaviour whereas the guided wave model is more complex. From the diagram, it can be seen that the transmission components, which provide information about the low spatial frequency components of the image (see for example [15]), match between the guided wave and acoustic models, enabling a low resolution image to be produced. However, in other scattering directions (closer to reflection, corresponding to high spatial frequency components) there is a significant difference in scattering behaviour, which prevents higher resolution components from being extracted for imaging.

Significant focus has been given to the development of velocity inversion schemes, utilising this assumption that acoustic scattering matches guided wave scattering behaviour. Dominating this is the use of ray theory in the inversion. Typically arrival times are extracted from the measured waves, then a ray model is fitted to these such that the modelled and measured arrival times match. This can use straight ray assumptions [1, 5, 16], although more recent approaches account for refraction by iteratively bending the ray paths [9, 11]. Resolution improvements are available through the use of diffraction tomography for velocity inversion [8], although this is only applicable to weakly scattering defects, i.e. ones which are low contrast and small. The HARBUT approach [17] overcomes this by combining ray tomography with diffraction tomography to enable the benefits of diffraction tomography to be realised across a wider range of defects, and was applied to guided wave tomography in [10]. Full wave inversion, where an acoustic finite difference model is iteratively updated to match the measurements, has also been used for this problem [12], although the approach is still restricted to acoustic, rather than guided wave, scattering and therefore is limited in the same way as other velocity inversion approaches.

To improve accuracy beyond this, approaches which can more accurately capture the guided wave scattering are needed. A simple enhancement is to consider density in addition to velocity when inverting [18], which can improve accuracy, but this still fails to capture guided wave scattering fully. In a more sophisticated approach, Rose et al. developed Mindlin plate theory [19] for guided wave tomography [20, 21]. Under this model the behaviour of the plate is modelled using three field parameters: two rotations and the out of plane displacement. The scattering from guided waves can be captured by this model, and the paper illustrates scattering patterns and discusses how this behaviour can be used in an inversion under the Born approximation to achieve a quantitative map of thickness. However, the approach assumes small perturbations in local properties, i.e. small wall losses,

and the use of the Born approximation severely limits the range of defects which can be modelled. Additionally, while Mindlin theory is undoubtedly an improvement on the guided-wave-to-velocity mapping assumption, it is a simplified model and therefore cannot capture the full scattering behaviour. Iterative solutions such as the Monte Carlo Markov Chain have been applied to this problem [22], but this was limited to very small scatterers due to the need to run the forward model many times. Other guided wave imaging approaches have been demonstrated, including the use of the linear sampling method [23], and techniques producing non-quantitative images [24].

This paper develops a new general model, fully capturing guided wave scattering, and develops an inversion technique based on this. The approach is based on the HARBUT algorithm [10, 17] and makes no restriction on the width or depth of the scatterers and generally provides results that have superior resolution and accuracy to the existing techniques. Section 2 discusses the theory, providing the background of the standard acoustic (i.e. non-guided-wave) scattering model which is then extended to enable scattering from guided waves to be captured. Section 3 then outlines approaches to invert the developed scattering model, with Sect. 4 presenting results from the algorithm. Section 5 discusses aspects such as stability and effects of density.

2 Scattering Theory

2.1 Standard acoustic model

The analysis begins with the standard acoustic model, widely used for many quantitative imaging problems, from which a more general approach will be derived which better captures complex scattering. The acoustic wave equation is written in the frequency domain

$$\left[\nabla^2 + k\left(\mathbf{x}\right)^2\right]\phi = 0 \tag{1}$$

where $k(\mathbf{x})$ is the local wavenumber at position $\mathbf{x}$ and ϕ represents the local acoustic scalar potential. This can be rearranged

$$\begin{aligned}\left[\nabla^2 + k_0^2\right]\phi &= -\left[k\left(\mathbf{x}\right)^2 - k_0^2\right]\phi &(2)\\ &= -O(\mathbf{x})\phi &(3)\end{aligned}$$

where k_0 is the background wavenumber, and the object function $O(\mathbf{x})$ has been introduced; this is normally expressed in terms of the velocity as

$$O(\mathbf{x}) = k_0^2\left[\left(\frac{c_0}{c(\mathbf{x})}\right)^2 - 1\right]. \tag{4}$$

Here, c_0 represents the background velocity and $c(\mathbf{x})$ the local velocity.

The acoustic free space Green's function can be derived as the solution to

$$\left[\nabla^2 + k_0^2\right]G\left(\mathbf{y},\mathbf{x}\right) = \delta\left(\mathbf{x}-\mathbf{y}\right) \tag{5}$$

which is solved by

$$G\left(\mathbf{y},\mathbf{x}\right) = -\frac{i}{4}H_0^{(1)}\left(k_0 R\right) \tag{6}$$

where

$$R = \left|\mathbf{x}-\mathbf{y}\right|$$

and $H_0^{(1)}$ is the Hankel function of the first kind. This is then exploited in the integral formulation [15, 25]

$$\phi_s\left(\mathbf{y}\right) = \phi\left(\mathbf{y}\right) - \phi_0\left(\mathbf{y}\right) = -\int G\left(\mathbf{y},\mathbf{x}\right)O\left(\mathbf{x}\right)\phi\left(\mathbf{x}\right)d\mathbf{x} \tag{7}$$

where the scattered field ϕ_s is derived in terms of the total field ϕ and the incident field ϕ_0.

Taking a point scatterer of scattering potential ρ at position $\mathbf{x}$, the integral reduces to

$$\phi_s\left(\mathbf{y}\right) = -G\left(\mathbf{y},\mathbf{x}\right)\rho\phi\left(\mathbf{x}\right) \tag{8}$$

which has a clear omnidirectional scattering behaviour visible due to the axisymmetric nature of G. It is well known that guided waves do not scatter like this [26, 27]. As shown in [14], it is the discrepancy between this acoustic scattering and the full guided wave scattering which limits the accuracy of the acoustic model and hence its resolution. To improve this, a more accurate scattering model is required.

2.2 Generalised scattering model

As discussed, the monopole scattering behaviour is unrealistic for capturing full guided wave scattering. Therefore higher orders are needed; these can be expressed as a sum of cosine terms in a variation on eq. (7)

$$\phi_s = \int GO\phi \sum_{m=0}^{M} C_m \cos(m\theta)\, d\mathbf{x} \tag{9}$$

where θ is the deviation angle between the illumination and reception direction and M is the highest order cosine term; for the omnidirectional acoustic case $M = 0$ is sufficient. The values C_m represent the coefficients associated with each cosine term and hence describe the scattering behaviour. It is noted that the added directionality term could be included in a Lamb wave Green's function, however the terms will be kept separately throughout this paper and G will always be used to refer to the 2D free space acoustic Green's function.

Defects across a wide range of depths (including beyond 50% wall loss) are of interest so it is not guaranteed that the scattering pattern will remain constant with depth. Therefore the model must be adjusted so that different scattering patterns can be expressed at different depths, which is achieved via a polynomial expansion of the object function in terms of the thickness parameter, $h(\mathbf{x}) = [T_0 - T(\mathbf{x})]/T_0$, with T_0 and T being background and local thicknesses respectively

$$\phi_s = \int G\phi \sum_{n=1}^{N} \sum_{m=0}^{M} C_{mn} h^n \cos(m\theta)\, d\mathbf{x}. \tag{10}$$

Here the coefficient term C_{mn} has been expanded to account for the N polynomial terms. This form of equation allows the scattering pattern to vary with depth. It is noted that, since scattering is not expected to originate from the background region where $h = 0$, there is no constant term so $n = 0$ is not included. While this equation represents an approximation due to the truncation of both the polynomial (n) and cosine (m) series, only low orders of both are typically required to capture the scattering behaviour.

To predict the scattering behaviour under this model, the coefficients C_{mn} must be estimated. Rearranging the equation gives

$$\phi_s = \sum_{n=1}^{N} \sum_{m=0}^{M} C_{mn} \int G\phi h^n \cos(m\theta)\, d\mathbf{x} \tag{11}$$

which can be rewritten

$$\phi_s = \sum_{n=1}^{N} \sum_{m=0}^{M} C_{mn} P_{mn} \tag{12}$$

with

$$P_{mn} = \int G\phi h^n \cos(m\theta)\, d\mathbf{x}. \tag{13}$$

To determine ϕ_s and P_{mn} a suitable forward model is needed. Traditionally, significant simplifying approximations were necessary to produce such data. However, the increasing computer power available makes running large sets of full finite element (FE) simulations practical. The Pogo FE software package [28] solves elastodynamic problems via an explicit time domain scheme, and is used here to simulate the wave interaction with defects. This approach captures the full guided wave scattering behaviour, enabling the field ϕ to be determined. By running a similar simulation without the scatterer present, the incident term ϕ_0 can be determined and subtracted from ϕ to give the scattered field ϕ_s away from the scatterer, and hence the left hand side of (12). The integral (13) is calculated using a sum across the domain $\mathbf{x}$ with a sufficiently small spacing (typically $\lambda/15$ is sufficient, depending on scatterer size, with λ being the wavelength). The terms in the integral are all straightforward to determine: G is known from (6), ϕ can be taken directly from the simulation, h is known from the thickness map and θ can be calculated from geometry.

Once ϕ_s and P_{mn} are known, C_{mn} can be extracted through the use of a linear solver to invert (12). Clearly there are actually many scattering scenarios, giving multiple data sets for P_{mn} and ϕ_s; even for just a single realisation of $h(\mathbf{x})$ both the scattering direction and the illumination direction will vary, giving many scattering values. Also it is desirable to have a solution which is valid across many different defects, so several defect sizes and depths will be simulated. Ultimately (12) will represent a highly overdetermined system of equations, and from this C_{mn} can be calculated in the least-squares sense.

2.2.1 Acoustic scattering with the generalised scattering model

To demonstrate the general scattering model, the acoustic case is returned to. This is simpler than a full guided wave case, and an analytical solution exists for comparison. An elemental scatterer under the acoustic model has omnidirectional scattering, so as discussed, only a single order cosine expansion is needed, i.e. $M = 0$. Therefore a set of coefficients C_{0n} are sought to solve

$$\phi_s = \sum_{n=1}^{N} C_{0n} P_{0n} \tag{14}$$

with

$$P_{0n} = \int G \phi h^n d\mathbf{x}. \tag{15}$$

It is noted here that while this is formulated in terms of the acoustic velocity, the velocity-to-thickness mapping from the dispersion curves, traditionally used in guided wave tomography, is used so that the h term retains its meaning. To test this, a frequency domain finite difference simulation is performed for several defects. This is operated at 50kHz using parameters from the A0 mode on a 10mm thick steel plate; node spacing was 1mm and 240 elements were used in a circular array around the defect. All defects were axisymmetric Hann defects as described in [18], and had widths of 20, 40, 60, 80 and 120mm, and depths of 10, 30, 40, 50, 55, 60% of wall thickness, making 26 simulations in total, including a run to obtain the incident field ϕ_0. The coefficients are then extracted from these scattered fields using the approach described previously.

There are likely to be two sources of error in the scattering behaviour predicted by these coefficients. Firstly, there is uncertainty in the modelling of the scattered fields and subsequent fitting of the coefficients to these, and secondly there is likely to be some truncation error due to fitting a polynomial to the function. It is possible to separate these and just study the truncation error. Since the scattering behaviour is well known analytically, the coefficients can be determined independently, without using the scattered field

$$-\int GO\phi d\mathbf{x} = \int G\phi \sum_{n=1}^{N} C_{0n} h^n d\mathbf{x} \tag{16}$$

$$-O = \sum_{n=1}^{N} C_{0n} h^n. \tag{17}$$

A direct approach to acquire C_{0n} involves calculating $O(h)$ then fitting the polynomial terms to it. The process for determining $O(h)$ is in two steps; firstly the phase velocity c, associated with the thickness, is derived by interpolating the dispersion curves, typically calculated via a tool such as DISPERSE [29]. Then O is calculated from that as in (4). Given the lack of simple analytical equation for the dispersion characteristics, the chosen approach is to numerically evaluate the function $O(h)$ across a range of thickness values from 0-60% wall loss; the polynomial coefficients are then used to fit this function.

Figure 3 shows the comparison between the true $O(h)$ term and two $\sum_{n=1}^{N} C_{0n} h^n$ terms for the coefficients calculated via the different approaches discussed here. The 'true' curve $O(h)$ is calculated semi-analytically as discussed above, and the 'direct' curve compares that to its polynomial approximation calculated directly as in (16). Comparing these two lines first, it is clear that the polynomial approximation does introduce small differences, however these appear small and would be unlikely to severely affect the accuracy of a reconstruction. This suggests that 3 polynomial terms is sufficient for this problem. The final line is calculated using coefficients extracted from the scattered field. Here, there is a slightly larger deviation at deeper depths (beyond 50% wall loss). One aspect to note is that this line and the true line match better for shallower defects, so there is a possibility that better fitting has been performed for the shallower depths. It is noted that because each defect varies from its maximum depth through to zero contrast, there average depth throughout each defect will be significantly less than the maximum. Therefore across all of the scattered fields the majority of the scattering will come from the shallower defect values; this is why bias was given to deeper defects in the simulations. However, there are still more shallower areas in total and this could explain why better fitting is obvious in this area. Additionally, as defects get deeper, more non-linearity tends to occur and the underlying assumptions (e.g. the lack of multiple scattering) will break down, which could cause larger errors. However, based on this study it is expected that the scattering model with 3 polynomial terms should be a good approximation for the majority of defects across the range of interest.

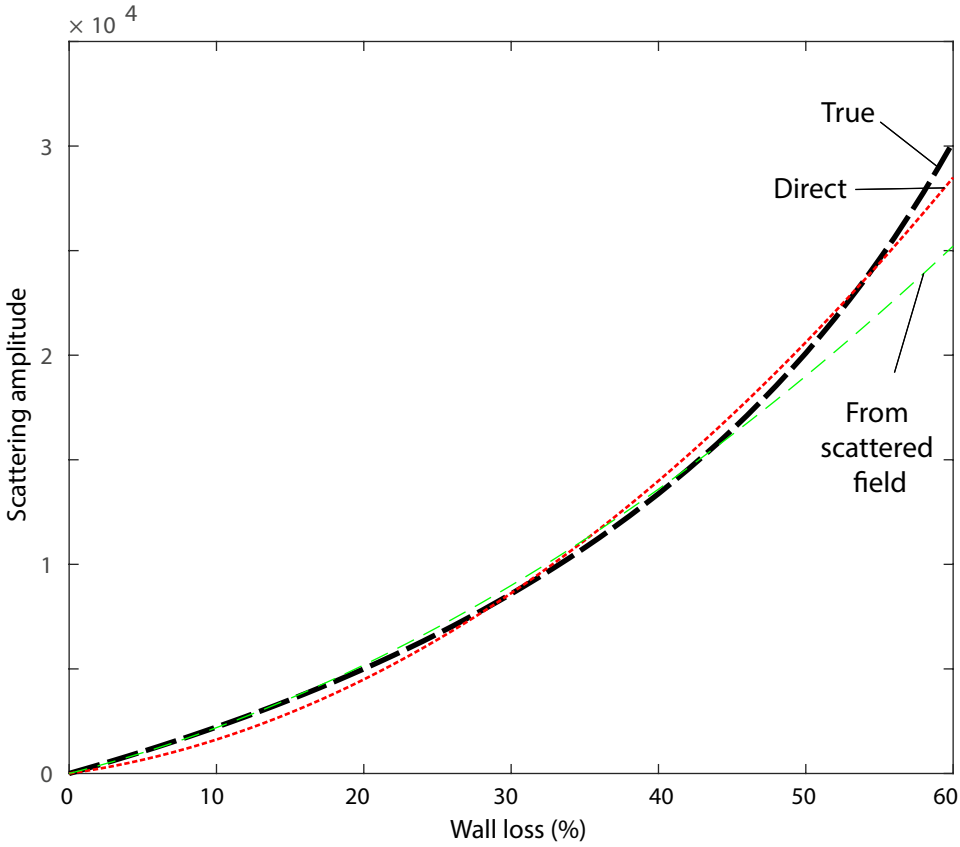

Figure 3: True and approximated scattering terms under the generalised scattering model applied to the standard acoustic scattering problem. The direct field utilises (16) to obtain the coefficients without generating any scattered fields, and compares this to the true scattering values defined by O. For the remaining line, several finite difference simulations were performed and the scattered field extracted from these. Coefficients are then extracted from these and used to produce the line.

2.2.2 Multi-modal generalisation

In many scenarios, scattering occurs in a medium which can support multiple modes, and in the majority of cases some mode conversion will occur. It is noted that the current formulation could, in theory, be used to capture such multi-modal behaviour

$$\phi_{sr} = \sum_{n=1}^{N} \sum_{m=0}^{M} \sum_{q=1}^{Q} C_{mnqr} P_{mnqr} \tag{18}$$

with

$$P_{mnqr} = \int G_r \phi_q h^n \cos(m\theta)\, d\mathbf{x}. \tag{19}$$

Here, q represents the incident modal wavefield with Q being the number of modes present. $1 \leq r \leq Q$ represents the measured mode. Clearly this formulation increases the number of parameters which need to be determined by a factor of Q^2, compared to the single mode case. While this description is included for completeness, it has not been tested in practice and a suitable inversion approach based on it has not been derived. A very similar approach to this has been discussed in [30], and as highlighted there and investigated in [31], a particular problem is that the K-space is not completely sampled by the combined two modes; a section of wavenumbers close to zero cannot be extracted. Another practical challenge is the complexity of experimentally measuring and exciting several different modes while maintaining ability to separate them.

2.3 Scattering behaviour

Figure 4 illustrates the scattering patterns associated with different depth 'elemental' defects, given by the equation

$$s(\theta) = \sum_{n=1}^{N} \sum_{m=0}^{M} C_{mn} h^n \cos(m\theta). \tag{20}$$

The coefficients in this case are derived for $M = 3$ and $N = 3$, and are calculated by fitting the responses from defects of a variety of widths and depths down to 60% wall loss following the approach in Sect. 2.2. It is observed that these results match those predicted analytically for shallow defects in [21] under Mindlin theory, which are further analysed in [30]. It is clear that in through-transmission the two curves generally match well, with increasing deviation with depth, matching the trend seen in Sect. 2.2.1, Fig. 3. This is more clearly highlighted in Fig. 4(g) showing the transmission component as a function of wall loss, with a very similar deviation to that visible before.

In reflection, the guided wave scattering does not match the acoustic scattering behaviour well; at 10% it is larger compared to the acoustic case, but it decreases in amplitude and between 30% and 40% wall loss becomes negative. Scattering at other angles is also very different. As illustrated in Fig. 4(h) there is a significant zero around 1 radian; despite the diversity of scattering behaviour with depth, at this angle the scattering amplitude remains zero for all depths. This can be problematic since the information contained in the scattered field at this angle is unavailable.

3 Inversion

The primary motivation for developing this model is to exploit it in inversions to generate improved images. This section begins with an overview of the diffraction tomography based approaches for acoustic problems.

3.1 Acoustic inversion

3.1.1 Diffraction tomography

Beginning from the Lippmann-Schwinger equation of (7)

$$\phi_s(\mathbf{y}) = -\int G(\mathbf{y}, \mathbf{x})\, O(\mathbf{x})\, \phi(\mathbf{x})\, d\mathbf{x} \tag{21}$$

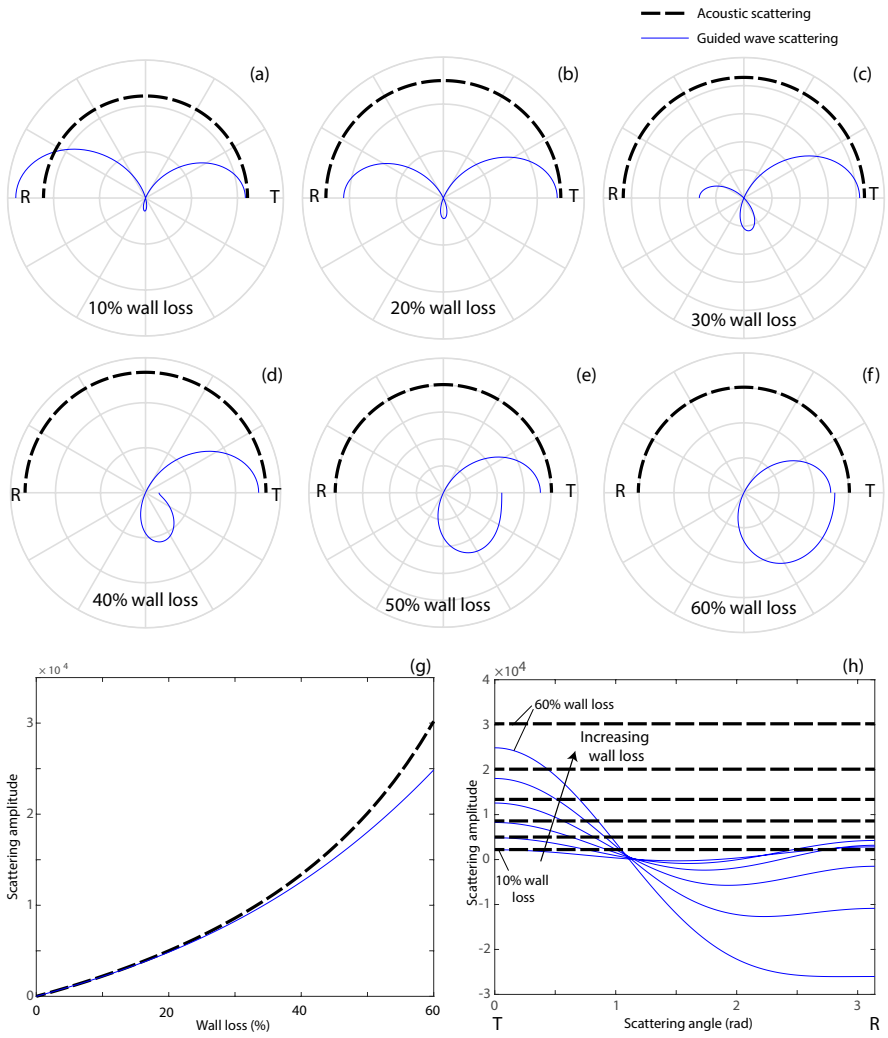

Figure 4: Scattering patterns for different depth elemental defects for guided waves and an equivalent acoustic model based on the dispersion curves. These are calculated for an operating point of 0.5 MHz-mm using A0. (a)-(f) show scattering patterns for defects of depth 10%, 20%, 30%, 40%, 50% and 60%. Due to the presence of negative values, scattering is only plotted from 0 to π radians. (g) plots the transmission components, comparing the acoustic case with the guided wave values for a 0 degree scattering angle. (h) plots the curves of (a)-(f) on a linear scale. T and R are used to indicate through-transmission and full (π radians) reflection respectively.

two simplifying assumptions are employed, firstly that of the Born approximation, that $\phi = \phi_0$ within the integral, and secondly that the transducer array is in the far field, so that plane wave assumptions hold; this leads to [15, 32]

$$A\left(\hat{\mathbf{s}}, \hat{\mathbf{s}}_\mathbf{0}\right) = \int O\left(\mathbf{x}\right) e^{-ik\left(\hat{\mathbf{s}}-\hat{\mathbf{s}}_\mathbf{0}\right).\mathbf{x}} d\mathbf{x} \tag{22}$$

where $\hat{\mathbf{s}}$ and $\hat{\mathbf{s}}_\mathbf{0}$ represent directions for the scattered and incident fields respectively and A is the far field scattering amplitude. It is clear that this represents a 2D Fourier transform

$$A\left(\hat{\mathbf{s}}, \hat{\mathbf{s}}_\mathbf{0}\right) = \hat{O}\left(\mathbf{K}\right) \tag{23}$$

where $\mathbf{K} = k(\hat{\mathbf{s}} - \hat{\mathbf{s}}_\mathbf{0})$, and by varying the incident and scattered directions all the wavenumber components of $\hat{O}$ in the range $|\mathbf{K}| \leq 2k_0$ can be determined. One approach is to acquire these components, interpolate them to a regular grid, then perform a 2D inverse Fourier transform to obtain O, as in

$$O\left(\mathbf{x}\right) = \frac{1}{4\pi^2} \int^{K_x} \int^{K_y} A\left(\hat{\mathbf{s}}, \hat{\mathbf{s}}_\mathbf{0}\right) e^{ik\left(\hat{\mathbf{s}}-\hat{\mathbf{s}}_\mathbf{0}\right).\mathbf{x}} dK_x dK_y \tag{24}$$

where K_x and K_y are the Cartesian components of the vector $\mathbf{K}$. Since this provides access to components up to $2k_0$ this corresponds to a resolution limit of $\lambda/2$ [32]. However, it is possible to avoid this interpolation. If the incident and scattered vectors are expressed as functions of angles, i.e. $\hat{\mathbf{s}} = \hat{\mathbf{s}}\left(\alpha\right)$ and $\hat{\mathbf{s}}_\mathbf{0} = \hat{\mathbf{s}}_\mathbf{0}\left(\beta\right)$ then a change of coordinates can be performed to give

$$O\left(\mathbf{x}\right) = \frac{1}{4\pi^2} \int^{\alpha} \int^{\beta} A\left(\hat{\mathbf{s}}, \hat{\mathbf{s}}_\mathbf{0}\right) e^{ik\left(\hat{\mathbf{s}}-\hat{\mathbf{s}}_\mathbf{0}\right).\mathbf{x}} W\left(\mathbf{K}\right) d\alpha d\beta \tag{25}$$

where W is a weighting function, corresponding to the determinant of the Jacobian matrix, to account for the change in coordinates; this is Devaney's filtered backprojection algorithm [33]. It can be shown [34] that this weighting function has the form

$$W\left(\mathbf{K}\right) = |\mathbf{K}|\, k_0 \sqrt{1 - \left(\frac{|\mathbf{K}|}{2k_0}\right)^2}. \tag{26}$$

One option is to compute this integral directly incorporating the weighting function. Alternatively it is recognised that this form is very similar to the standard beamforming (or total focusing method [35]) approach of delaying and summing around the array, which in the far field integral form would become

$$O\left(\mathbf{x}\right) = \int^{\alpha} \int^{\beta} A\left(\hat{\mathbf{s}}, \hat{\mathbf{s}}_\mathbf{0}\right) e^{ik\left(\hat{\mathbf{s}}-\hat{\mathbf{s}}_\mathbf{0}\right).\mathbf{x}} d\alpha d\beta \tag{27}$$

i.e. matching (25) with the exception of the weighting function. Rose et al. have conducted a thorough study of the behaviour of these different algorithms [36], and as explored in [37] this approach amplifies the low and high spatial frequency components in the image; this effect can be removed by applying a filter to generate the standard diffraction tomography image. One benefit of this approach is that beamforming images do not rely on the far field (plane wave) assumption; since the same image can be generated regardless of transducer location, the same diffraction tomography image will be generated from near- or far-field data. As highlighted previously [8] there is often also no need for incident field subtraction with this approach, a traditional difficulty with diffraction tomography. This approach is taken as the basis for the solutions developed in this paper.

3.1.2 HARBUT

As highlighted in [14], the capabilities of diffraction tomography are limited for guided wave tomography because the typical defect sizes generate sufficient phase shift through them that Born approximation is violated (i.e. ϕ_0 is not a good approximation of ϕ). Instead, HARBUT (Hybrid Algorithm for Robust Breast Ultrasound Tomography) [17, 38] is employed. This splits the object function into two components

$$O = O_\delta + O_b \tag{28}$$

where O_b corresponds to an approximate, known background estimate of O, typically estimated from bent ray tomography or a previous HARBUT iteration, and O_δ corresponds to the small, low contrast residual. Since O_δ

is low contrast, the Born approximation should be suitable for reconstructing it against the known background O_b. By reformulating the equations of Sect. 2.1 for this (see [17] for details) the scattering equation becomes

$$\phi - \phi_b = \phi'_s = -\int G_b O_\delta \phi d\mathbf{x} \tag{29}$$

which is approximated by

$$\phi'_s = -\int G_b O_\delta \phi_b d\mathbf{x} = -\int G_b O_\delta G_b d\mathbf{x} \tag{30}$$

where subscript b is used to indicate the values of the scattered field and Green's functions in the background, and it has been recognised that the background field can be calculated using the Green's function. The inversion is then performed in a similar way to before

$$O'_\delta = -\int^\alpha \int^\beta \frac{\phi}{G_b G_b} d\alpha d\beta \tag{31}$$

for a beamforming image, which is then filtered to the diffraction tomography version to give the true O_δ value. Clearly the terms G_b need to be calculated; these are derived as being the same as the standard Green's functions (6) except with a phase distortion accounting for the background, calculated by using a fast eikonal equation solver [39]. It was shown that iterating HARBUT [10] can enable improved reconstructions to be achieved as O_δ reduces in amplitude and ϕ_b becomes a better approximation of ϕ. HARBUT has been shown to produce the best results based on the acoustic assumption across a range of defects [14], and will therefore be developed to account for the full guided wave scattering behaviour.

3.2 Elastic guided wave inversion

Several techniques are possible, based on these methods, to derive a solution to invert guided wave data. Two approaches are explored initially, which will introduce concepts which are ultimately combined into a single algorithm to address the problem.

3.2.1 Fourier component weighting

One simplifying assumption in the scattering model which could be made is that

$$C_{mn} = A_m B_n \tag{32}$$

i.e. that the polynomial terms are separable from the cosine terms. Based on this

$$s(\theta) = \sum_{n=1}^{N} \sum_{m=0}^{M} C_{mn} h^n \cos(m\theta) = \sum_{n=1}^{N} B_n h^n \sum_{m=0}^{M} A_m \cos(m\theta) \tag{33}$$

which demonstrates that the assumption is effectively forcing the scattered field to be the same shape regardless of depth. As shown in Sect. 2.3 this is not a good assumption across the range of defects considered here, however for shallow defects this may be valid, such as when Mindlin theory holds [21]. Under the far field Born approximation, Eq. (22) becomes

$$\phi_s = -\int e^{ik(\hat{\mathbf{s}}-\hat{\mathbf{s}}_\mathbf{0}).\mathbf{x}} \sum_{n=1}^{N} B_n h^n \sum_{m=0}^{M} A_m \cos(m\theta)\, d\mathbf{x} \tag{34}$$

and the polynomial and cosine terms can be separated in the inversion

$$O = \sum_{n=1}^{N} B_n h^n = -\frac{1}{4\pi^2} \int^\alpha \int^\beta \frac{\phi_s\left[k(\hat{\mathbf{s}}-\hat{\mathbf{s}}_\mathbf{0})\right] e^{-ik(\hat{\mathbf{s}}-\hat{\mathbf{s}}_\mathbf{0}).\mathbf{x}} W(\mathbf{K})}{\sum_{m=0}^{M} A_m \cos(m\theta)} d\alpha d\beta. \tag{35}$$

The approach is to perform the inversion in the standard manner, with an additional weighting term resulting from the cosine functions; this approach is similar to that developed by Rose et al. [21]. This solution gives O, and then h must be determined by inverting $O = \sum_{n=1}^{N} B_n h^n$. Following the standard guided wave tomography

approach of interpolating the dispersion curves to determine thickness from velocity, it is proposed that this could be solved by calculating $O(h)$ for a set of sufficiently sampled values of h in the range $0 \leq h \leq 1$, which can then be interpolated for each value of O to give h.

One challenge of solving eq. (35) is the division by $\sum_{m=0}^{M} A_m \cos(m\theta)$ required by the weighting; as shown in Sect. 2.3 there are clear angles when the scattered field is zero, which will result in a singularity. It should be possible to compensate for this by adding an arbitrary small constant to avoid the denominator ever becoming zero although this will cause small errors in the reconstruction. Alternative solutions could be to combine multiple frequencies, where the singularity will occur at different $|\mathbf{K}|$ values, thus enabling information which is unavailable at one frequency to be replaced with information from another. It is possible to incorporate the $\sum_{m=0}^{M} A_m \cos(m\theta)$ terms into a filter to be applied to a beamforming image; this has similar advantages to before by enabling near-field imaging and avoiding the incident field subtraction problem. The application of this filter is described by an operator

$$O_{gw} = \mathfrak{P}(O_{ac}) \tag{36}$$

which converts a reconstructed acoustic object function O_{ac} to a guided wave version O_{gw}.

This can be generalised to HARBUT. For the first iteration, the background object function O_b only contains low frequency components, generated by a ray-tomography algorithm; these correspond to the transmission subset and as shown in Sect. 2.3 the acoustic model matches the guided wave model well in this area, i.e.

$$O_b \approx \mathfrak{P}(O_b). \tag{37}$$

When calculating the residual, O_δ, the weighting will need to be applied and this can either be applied immediately

$$O_{gw} = \mathfrak{P}(O_{\delta,ac}) + O_b \tag{38}$$

or after adding the background object function

$$O_{gw} = \mathfrak{P}(O_{\delta,ac} + O_b) \tag{39}$$

both of which should generate the same result because of (37). These two approaches can be utilised for iterative HARBUT. Each contribution of O_δ can either be filtered immediately or at the end when they have been summed up. In the latter case, because the corrections are not applied before the corrected steering functions are calculated, there will be slight distortions to the wavefields G_b, however it is generally the low spatial frequency components which are the most important in these calculations (and in fact the background is generally smoothed prior to calculating G_b [10]) so any differences will be negligible.

3.2.2 Iterative solution

As discussed, the assumption that the scattering behaviour is constant with defect depth is not valid for the ranges considered here. The complexity therefore increases significantly, because the algorithm must account for the different scattering behaviour with depth without knowledge of what the depth is. One of the most straightforward approaches would be to utilise a least squares minimisation based on the scattered field, minimising a cost function defined as

$$F = \sum |\phi_{s,model} - \phi_{s,meas}|^2 = \sum |r|^2 \tag{40}$$

where $\phi_{s,meas}$ is the measured scattered field and $\phi_{s,model}$ corresponds to the modelled scattered field, as generated from (10), and $r = \phi_{s,model} - \phi_{s,meas}$ is the residual. A gradient approach can be used to achieve this, and an efficient gradient calculation method can produce this derivative relative to the values of h in the image. This is expressed as

$$\frac{\partial F}{\partial h(\mathbf{x})} = \sum 2r \frac{\partial \phi_{s,model}}{\partial h(\mathbf{x})} \tag{41}$$

and the derivative of the scattered field, based on the generalised scattering model, is calculated as

$$\frac{\partial \phi_{s,model}}{\partial h(\mathbf{x})} = G\phi \sum_{n=1}^{N} \sum_{m=0}^{M} C_{mn} n h^{n-1} \cos(m\theta). \tag{42}$$

With the exception of ϕ, these terms are all known. ϕ can be determined from any of a number of forward solutions (e.g. finite difference or finite element) based on the current thickness map; probably the fastest approach would

be to follow the HARBUT formulation [17] with an eikonal solver to distort the incident field. Having calculated this gradient, a solution technique such as the conjugate gradient method could be utilised to minimise the cost function by stepping to minimise it. While this approach has been included for completeness, it is not taken further because it requires incident field subtraction to produce $\phi_{s,model}$ and is potentially slow since the sums of (42) need to be calculated at every location $\mathbf{x}$ in the image for every iteration. However, the concept of least-squares fitting explored in this section can be combined with the Fourier component weighting approach discussed above, as will be explored in the next section.

3.2.3 HARBUT with an Improved Scattering Model (HARBUTISM)

As discussed above for the separable variables case, the standard acoustic reconstruction will contain all the components of the true reconstruction, just distorted. When the variables are not separable this still holds, but there is now no simple procedure to correct for the complex scattering behaviour since the depths are unknown. The least-squares fitting approach is again proposed, this time minimising the cost function

$$F_2 = \sum \left| \hat{O}_{ac} - \hat{O}_h \right|^2 = \sum |r_g|^2 \tag{43}$$

where $\hat{O}_{ac}$ is the 2D Fourier transform of the object function directly generated by HARBUT; the use of HARBUT at this point has corrected for wave distortions and any non-far field effects in the measurements, however it will still contain the complexities of guided wave scattering. Therefore the equivalent fitted to it must also account for the guided wave scattering behaviour, but can be produced using a far field Born approach. The equivalent $\hat{O}_h$ can be derived from the current thickness map using the improved scattering model, and by considering each $\mathbf{K}$ value in terms of plane wave illuminations and far field measurements applied to (10)

$$A\left(\hat{\mathbf{s}}, \hat{\mathbf{s}}_\mathbf{0}\right) = \int e^{-ik(\hat{\mathbf{s}}-\hat{\mathbf{s}}_\mathbf{0}).\mathbf{x}} \sum_{n=1}^{N} \sum_{m=0}^{M} C_{mn} h^n \cos\left(m\theta\right) d\mathbf{x} \tag{44}$$

which can be remapped to give $\hat{O}_h$

$$\hat{O}_h\left(\mathbf{K}\right) = \int e^{-i\mathbf{K}.\mathbf{x}} \sum_{n=1}^{N} \sum_{m=0}^{M} C_{mn} h^n \cos\left(m\theta\right) d\mathbf{x}$$

where it is noted that the scattering angle θ will be a function of $\hat{\mathbf{s}}$ and $\hat{\mathbf{s}}_\mathbf{0}$ and hence $\mathbf{K}$.

The gradient is calculated, as before, relative to $h\left(\mathbf{x}\right)$

$$\frac{\partial F_2}{\partial h\left(\mathbf{x}\right)} = \sum 2 r_g \frac{\partial \hat{O}_h}{\partial h\left(\mathbf{x}\right)} \tag{45}$$

with

$$\frac{\partial \hat{O}_h}{\partial h\left(\mathbf{x}\right)} = \sum_{n=1}^{N} \sum_{m=0}^{M} C_{mn} n h^{n-1} \cos\left(m\theta\right) e^{i\mathbf{K}.\mathbf{x}}. \tag{46}$$

Combining the two equations gives

$$\frac{\partial F_2}{\partial h\left(\mathbf{x}\right)} = \sum 2 r_g \sum_{n=1}^{N} \sum_{m=0}^{M} C_{mn} n h^{n-1} \cos\left(m\theta\right) e^{i\mathbf{K}.\mathbf{x}} \tag{47}$$

$$= 2 \sum_{n=1}^{N} \sum_{m=0}^{M} C_{mn} n h^{n-1} \sum r_g \cos\left(m\theta\right) e^{i\mathbf{K}.\mathbf{x}} \tag{48}$$

where it can be noted that the final summation is a discrete 2D Fourier transform of $r_g \cos\left(m\theta\right)$.

This approach will be referred to as HARBUTISM, HARBUT with an Improved Scattering Model. There are a number of advantages to this approach. It is much faster; the 2D Fourier transform significantly reduces the time taken compared to the multiple sums required previously. The approach also means that the advantages of HARBUT are maintained: it can generate accurate images with a wide range of defects and does not require the incident field to be subtracted. Also the singularity problem discussed for the separable variables case is

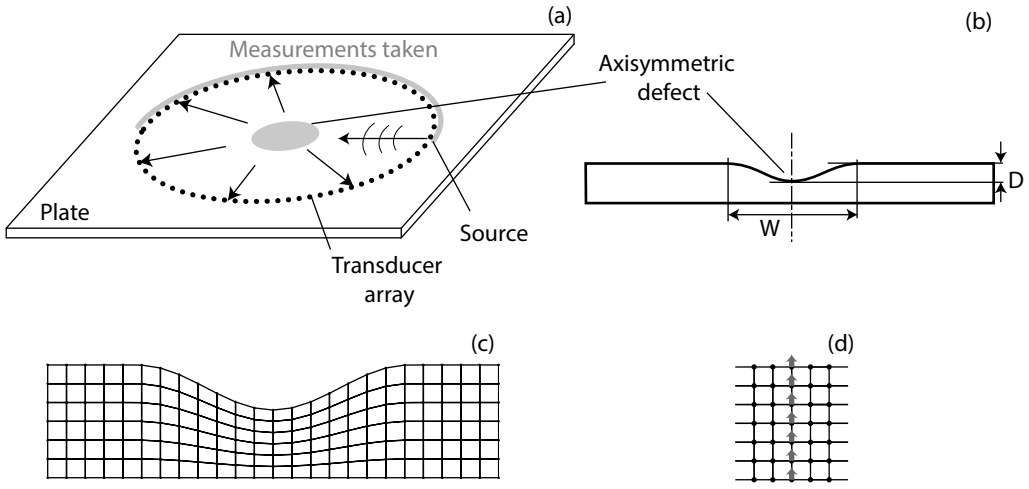

Figure 5: Configuration of the scattering setup. (a) shows the physical setup, with a source illuminating the axisymmetric defect and measurements taken around the array. The grey area marks the region where experimental data is acquired. (b) shows a cross section, defining the parameters D (depth) and W (width). (c) shows the finite element meshing approach and (d) illustrates how the A0 mode is excited in the plate.

minimised because division by the scattering pattern is not required. Instead, the two fitted functions will both have low amplitude components at particular values of $|\mathbf{K}|$ corresponding to the angle where scattering reaches zero, however the issues arising from this can be compensated for via regularisation approaches or combining multiple frequencies as mentioned previously.

In this paper, regularisation is applied at each iteration of the gradient descent algorithm to aid convergence. Two forms of regularisation are used: positivity and filtering. Positivity exploits the prior information that it is not possible to have negative wall loss, i.e. the plate thickness cannot increase, only decrease. This provides a restriction on what the wall loss values can be; therefore at each iteration the image is forced to match this restriction by setting any values $h < 0$ to 0. Filtering can remove spurious unwanted high spatial frequency components. Filtering is applied within HARBUT anyway, as part of the beamforming to diffraction tomography filter [37]; this removes any wavenumber components above the fundamental $2k_0$ limit. In fact, the filter cut-off values are selected to be slightly lower than this, to $1.7k_0$, sacrificing resolution to improve stability. This filter is also applied in HARBUTISM at every time step in order to minimise high spatial frequency artefacts.

It is noted that gradient descent methods as proposed here can suffer from convergence to local, rather than global, minima. However, the starting point of the iterative process is the HARBUT reconstruction, which has been shown to generally be close to the true solution. Analysis in this paper will evaluate several simple cases and two complex defects, providing a degree of confidence that local minima do not cause a problem, however future work may evaluate the stability of the algorithm across a much larger set of scenarios.

4 Results

The test cases presented here are similar to those used previously in [14, 18], so only the key parameters are given here. In all examples, the A0 mode has been used at 50kHz on a 10mm thick steel plate, although results are normalised to be valid for other thicknesses, provided the frequency is adjusted to ensure the same frequency-thickness product.

4.1 Simple defects

The configuration is illustrated in Fig. 5. As shown in Fig. 5(a) the array surrounds the defect and has radius 180mm, with 240 transducers. Axisymmetrical Hann-shaped defects were used, with thickness functions defined as

$$h\left(\mathbf{x}\right) = \begin{cases} 1 - \frac{D}{2}\left[1 + \cos\left(\frac{2\pi|\mathbf{x}|}{W}\right)\right] & |\mathbf{x}| < W/2 \\ 1 & |\mathbf{x}| \geq W/2 \end{cases} \tag{49}$$

for a defect of fractional depth D and width W. Due to symmetry, only a single illumination was needed, and the information from that could be replicated to make a complete data set containing all the send-receive combinations. The finite element software package Pogo [28] was used to simulate the different defects, with a uniform structured mesh squashed to model the defects as shown in Fig. 5(c). At the frequencies used, only the A0 and S0 modes are present, so the antisymmetric source shown in Fig. 5(d) was used to excite pure A0. Data from these simulations is included as electronic supplementary material.

Figure 6 presents the results for defects of different widths and depths. Overall it is clear that the accuracy is improved by using the improved scattering model in HARBUTISM versus relying on the acoustic to velocity mapping approach of HARBUT. This is particularly notable for narrower defects, indicating a resolution improvement; this fits with the observed resolution limit of the velocity-to-thickness mapping approach of around 2λ first identified in [14]. With the deeper defects, larger errors are typically visible. The polynomial approximation will inevitably contain more errors for the larger values of h where the truncation errors become larger; this will introduce errors both when calculating the coefficients C_{nm} and when using them in the inversion scheme. HARBUTISM can generally be expected to perform best for shallower defects.

4.1.1 Experimental comparison

Data from the two axisymmetric experimental cases of [14] were used for experimental validation. The defects had widths of 120mm and 60mm, and depths of 6mm and 3mm respectively. Measurements were taken around half the array with a laser vibrometer at 129 locations, as illustrated in Fig. 5(a), and replicated to give a full array, ultimately forming an array of 256x256 measurements.

Figure 7 presents the experimental results, with the equivalent simulated versions repeated for comparison. For both defects it is clear that the experimental data shows the same trends visible in the simulations. For the smaller defect, HARBUTISM clearly avoids the resolution limit present in HARBUT. In both experimental data sets HARBUTISM tends to overshoot more than the simulated equivalent, but this is generally by a small amount. It is likely that this has come from experimental uncertainties such as potential anisotropy present in the plate. Another potential source of errors is the data replication process. Because of this, noise, which would normally be incoherent between measurements, and hence be largely cancelled in the final image, is now coherent and forms axisymmetric ring artefacts as seen in [10]. It could be expected that such artefacts could also be superposed onto the defect reconstruction itself, affecting the accuracy.

4.2 Complex defect

The initial tests have demonstrated the performance of HARBUTISM for both simulated and experimental defects. However, it is important to test its behaviour when being extended to a fully complex defect. For these purposes, a laser scan of a real corrosion defect is used. This is scaled to make its maximum depth 50% of wall thickness, and the resulting thickness map is illustrated in Fig. 8(a). As before, a full finite element simulation is performed; this time, however, it is necessary to simulate all 240 sources in order to fully capture the field since there is no symmetry.

The reconstruction using the standard velocity-thickness mapping, calculated with HARBUT, is shown in Fig. 8(b). Clearly significant detail is missing from this reconstruction compared to the true thickness map. When full guided wave scattering is accounted for with HARBUTISM, Fig. 8(c), more of the finer features are visible in the reconstruction. Importantly, the deepest part of the defect is now a lot closer to being accurately captured by the imaging method. This is validated in the cross section through the deepest point of the defect, shown in Fig. 8(d). From this it is clear that the error between HARBUTISM and the true depth is less than 10%, while the HARBUT error is closer to 18%. This is largely caused by the differences in resolution between the two methods.

Resolution can be analysed by looking at the spatial frequency components. These are obtained by performing a 2D discrete Fourier transform on the values of h for the true, HARBUT and HARBUTISM images of Fig. 8; the results are shown in Fig. 9. It is clear that HARBUTISM extracts significantly more spatial frequency components than standard HARBUT. Quantifying resolution is challenging from such plots, but it is estimated that HARBUT can extract components in the range $|\mathbf{K}| < 0.6$, while HARBUTISM achieves around double this, $|\mathbf{K}| < 1.2$, corresponding to a resolution limit of less than λ. This is worse than the theoretical limit $|\mathbf{K}| < 2$; in part this is caused by the regularisation filter removing components above $|\mathbf{K}| = 1.7$, but also likely to be related to the challenges of accurately extracting and imaging from the very weak components scattered in the reflection subset of the data. Future work may examine approaches to reach this limit.

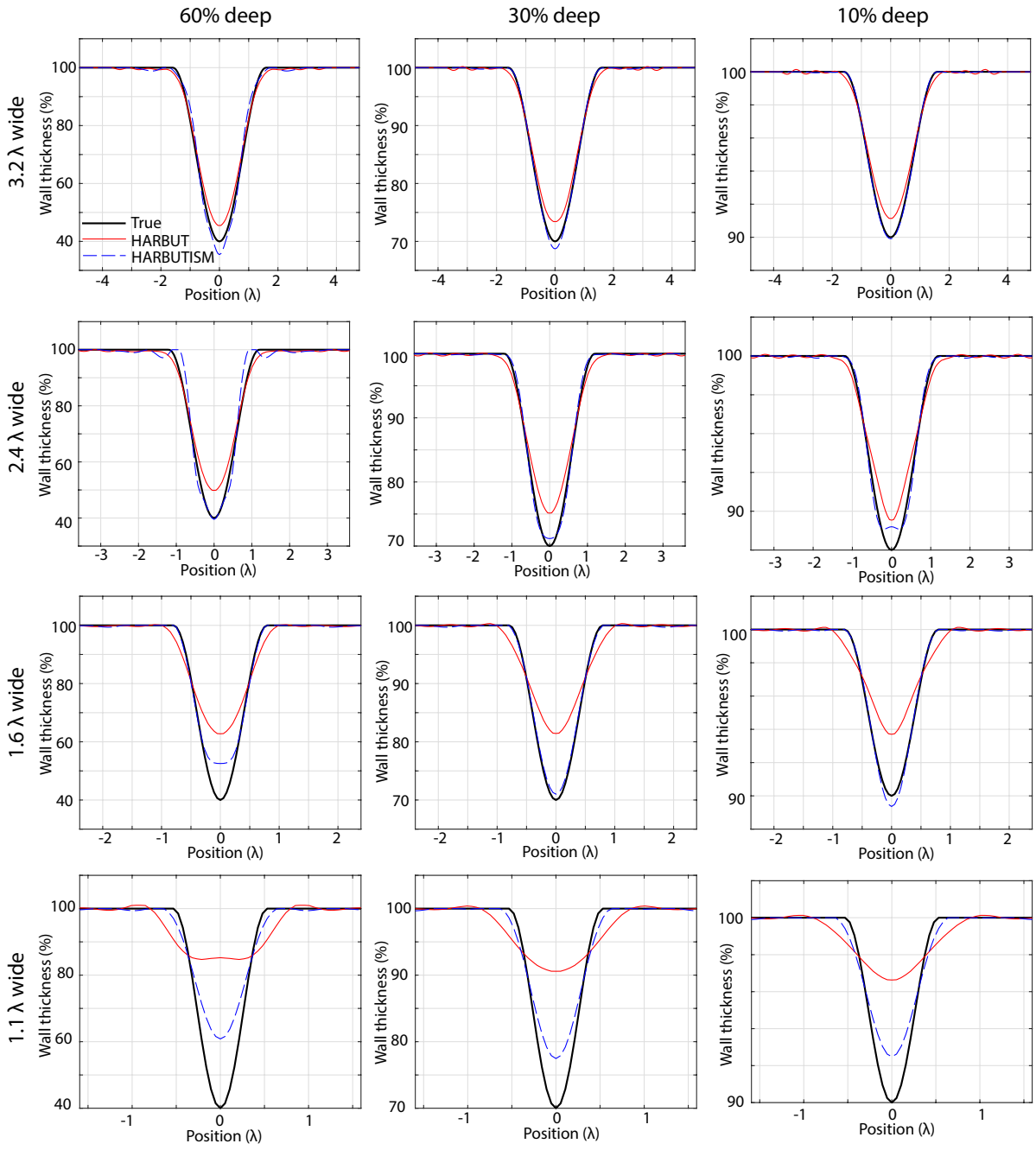

Figure 6: Cross sections across the axisymmetric defects for depths of 10%, 30% and 60%, and widths of 3.2, 2.4, 1.6 and 1.1 wavelengths. The true wall thickness is shown with a thick solid line, HARBUT in solid thin line and HARBUTISM with a dashed line.

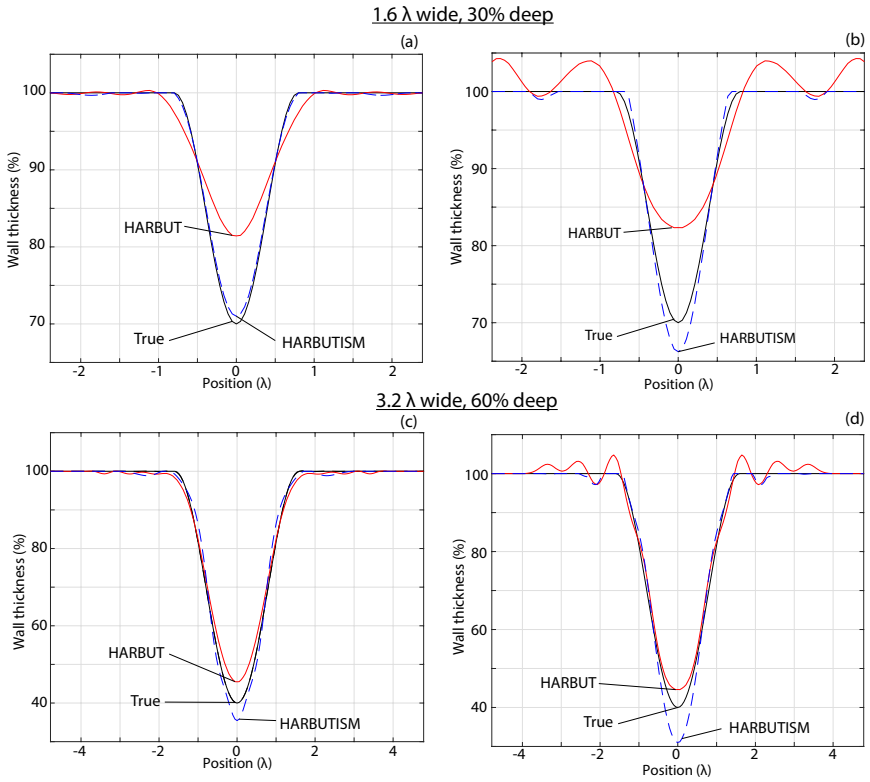

Figure 7: Experimental results. (a) and (b) show the 30% wall loss defect of width 60mm (1.6λ) and (c) and (d) present the 60% wall loss defect with width 120mm (3.2λ).

A further example has been tested to examine this. This is shown in Fig. 10(a) and consists of several axisymmetric Hann shapes superposed. As before, the HARBUT resolution is limited (Fig. 10(b)), while HARBUTISM is more accurate (Fig. 10(c)). The spatial frequency components of Figs. 10(d)-(f) show similar results to before, with HARBUT accurately capturing details up to around $|\mathbf{K}| < 0.6$. However, for this defect, HARBUTISM appears to produce a higher resolution reconstruction, up to around $|\mathbf{K}| < 1.6$, close to the regularisation filter level. It is unclear at present exactly why this case achieves better results. Notable differences include the shape being simpler than the real corrosion patch, the in-plane extent being smaller, and also the depth being slightly less than before, and it may be one of these which is related to the improvement.

One feature to note in Fig. 10(e) is the darker circle marked with the arrow, which is not visible in either of the other spatial frequency spectra. This occurs at a constant value of $|\mathbf{K}|$ and therefore corresponds to a particular scattering angle. This angle is an angle at which no scattering occurs from the guided waves, and matches the zero identified in Fig. 4(h).

4.2.1 Speed

HARBUTISM has not been highly optimised for speed; potentially there could be good savings from using the high parallelism of GPU (Graphical Processing Unit) technology for this task. However, even in its current form, written in Matlab, it runs at an acceptable speed. For the initial complex case, running on an HP Z820 workstation with 4 8-core Intel E5-2665 Xeon processors operating at 2.4GHz, the ray tomography time was 2.3s, standard HARBUT took 12.7s in addition to this, then HARBUTISM took a further 18.0s, making a total of 33s to generate a full image of a complex defect. This indicates that the system can deliver accurate images in a practical time-frame.

An alternative approach to solving this problem is to use a full numerical model to generate data, then iteratively update it until the numerical data matches the measured data. This could be done via a gradient descent approach or with one of the many approaches to sample the parameter space in order to find a global minimum. Either approach requires the full model to be run many times to match the two data sets. However, a complete forward model, even on multiple GPUs with Pogo [28], typically takes many hours or days to produce

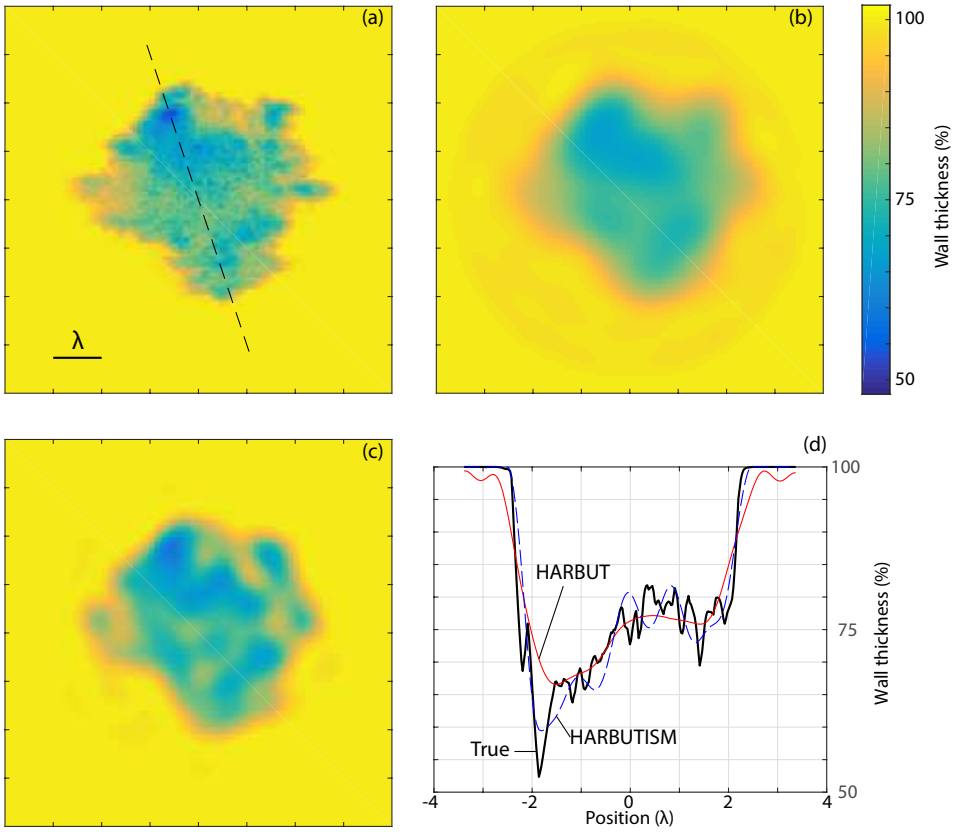

Figure 8: Results from a complex defect. (a) shows the true thickness map. (b) shows the standard HARBUT reconstruction and (c) HARBUTISM. (d) plots the cross section through the defect, on the line marked in (a).

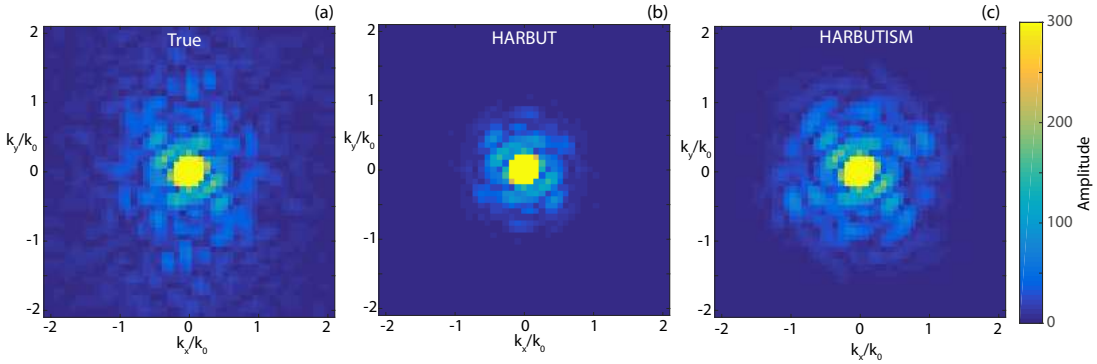

Figure 9: Spatial frequency components of the complex defect from Fig. 8. Amplitude has been clipped to enable lower amplitude values to be visible. (a) shows the components of the true map, (b) shows standard HARBUT and (c) presents HARBUTISM.

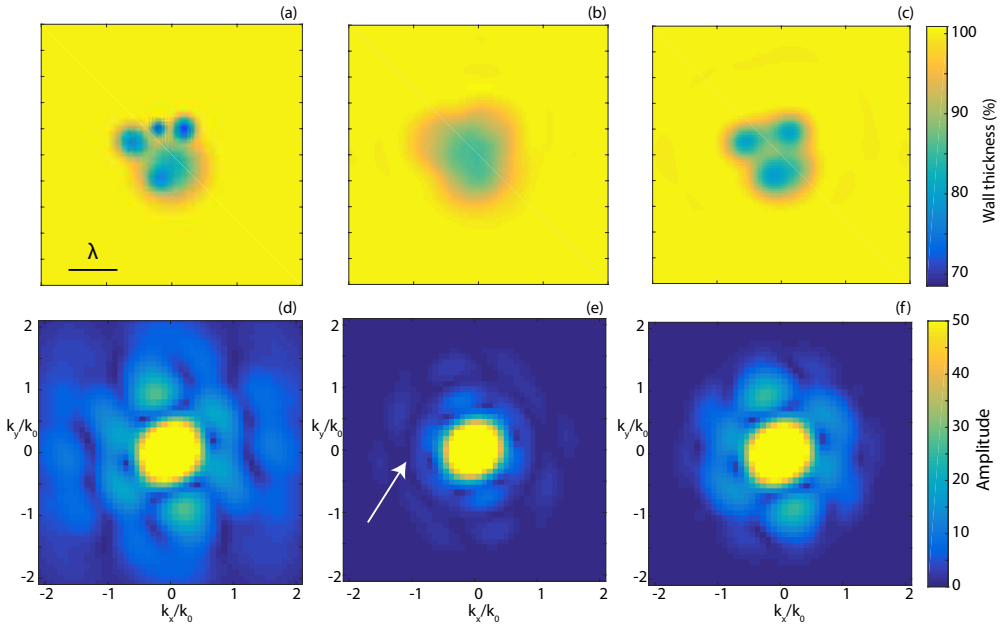

Figure 10: Artificial complex example. (a) shows the true map, (b) the HARBUT reconstruction and (c) HARBUTISM. (d)-(f) give the respective spatial frequency spectra, with amplitude clipped to enable lower amplitude details to be visible.

a full data set, and this must be repeated many times to achieve convergence. Even with the rapid pace of computational improvements, it is unlikely that this approach will be a practical solution for guided wave tomography in the foreseeable future.

5 Discussion

5.1 Density effect

A recent paper [18] discussed the effects of density in guided wave scattering, and highlighted how it can cause critical errors in the reconstruction if neglected. It is noted that this is the effective density that the guided wave experiences, rather than the material density; this effective density term is proportional to thickness. The improved scattering model has so far not explicitly accounted for density, so the effects of it will now be explored.

The definition of the object function incorporating density is defined as [40]

$$O(\mathbf{x}) = k_0^2 \left[\left(\frac{c_0}{c(\mathbf{x})} \right)^2 - 1 \right] - \rho^{1/2}(\mathbf{x}) \nabla^2 \rho^{-1/2}(\mathbf{x}) \tag{50}$$

where $\rho(\mathbf{x})$ is the local density. For simplicity in this analysis, it is assumed that thickness (and hence density) changes are small and that $\rho^{1/2}(\mathbf{x}) = \rho_r(\mathbf{x}) = \rho_{r0} + \delta\rho_r(\mathbf{x})$ where ρ_r has been introduced to signify the square root of density. The density component of the object function then becomes

$$\begin{aligned} O_\rho &= -(\rho_{r0} + \delta\rho_r) \nabla^2 (\rho_{r0} + \delta\rho_r)^{-1} && (51) \\ &\approx \rho_{r0} \nabla^2 \delta\rho_r && (52) \end{aligned}$$

where a truncated Taylor series has been used to expand $(\rho_{r0} + \delta\rho_r)^{-1}$. Since, under the far field Born approximation, the scattered field can be mapped to the Fourier transform of the object function, the density component of scattering can be written as

$$\phi_{s\rho}(\hat{\mathbf{s}}, \hat{\mathbf{s}}_\mathbf{0}) = \hat{O}_\rho \left[k_0 (\hat{\mathbf{s}} - \hat{\mathbf{s}}_\mathbf{0}) \right]. \tag{53}$$

The Laplacian term is a 2D second order spatial derivative so

$$\hat{O}_\rho(\mathbf{K}) = \mathfrak{F}\left(\rho_{r0} \nabla^2 \delta\rho_r\right) = -\rho_{r0} |\mathbf{K}|^2 \mathfrak{F}(\delta\rho_\mathfrak{r}) \tag{54}$$

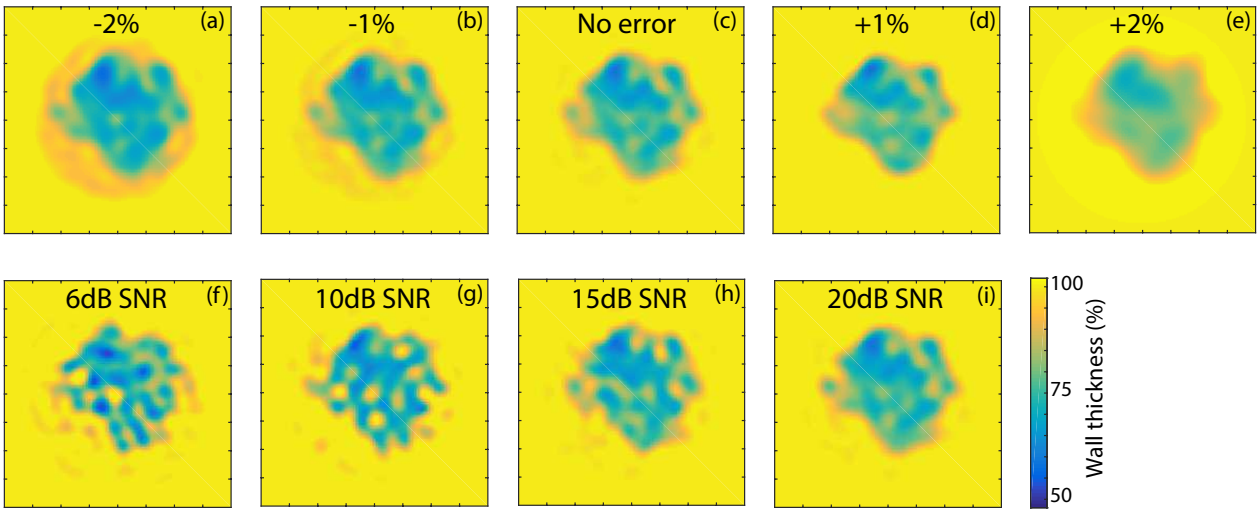

Figure 11: Effect of different errors on the HARBUTISM reconstruction of the complex defect from Sect. 4.2. (a), (b), (d) and (e) show systematic errors, scaling the transducer positions given to the algorithm by offsets of -2%, -1%, 1% and 2% respectively. (c) is included for reference, and is the case where no scaling is performed, i.e. no error is introduced. (f)-(i) present different levels of incoherent random noise, giving signal-to-noise (SNR) ratios of 6dB, 10dB, 15dB and 20dB respectively.

where $\mathfrak{F}$ indicates the forward 2D Fourier transform. Then

$$\hat{O_\rho}\left(\mathbf{K}\right) = -\rho_{r0}k_0^2\left|\hat{\mathbf{s}} - \hat{\mathbf{s}}_\mathbf{0}\right|^2 \mathfrak{F}\left(\delta\rho_\mathfrak{r}\right) \tag{55}$$

which, from geometry, can be expressed in terms of the scattering angle θ as

$$\hat{O_\rho}\left(\mathbf{K}\right) = -4\rho_{r0}k_0^2 \sin^2\frac{\theta}{2}\mathfrak{F}\left(\delta\rho_\mathfrak{r}\right) \tag{56}$$

$$= -2\rho_{r0}k_0^2\left(1-\cos\theta\right)\mathfrak{F}\left(\delta\rho_\mathfrak{r}\right) \tag{57}$$

using the half-angle identities. By expressing the equation in this way, it is clear that the Laplacian term is equivalent to introducing a directionality into the scattering, which can be expressed as a sum of $\cos m\theta$ terms. Similarly the $\delta\rho_r$ term can be approximated easily by a polynomial in h^n. This behaviour can therefore be captured by the generalised scattering model, and will automatically be accounted for in the coefficients extracted from the simulation. This integrated technique is arguably a more elegant solution for density correction compared to the previous approach [18] where an initial thickness map was generated ignoring density, then iteratively updated with a correction term based on the implied density.

This analysis has been performed using the assumption that the thickness variations were small, allowing the equations to effectively be linearised. However, for the deeper defects, it is likely that the density scattering behaviour will be similar, and therefore the improved scattering model should still be able to capture the behaviour, provided it has enough coefficients. It is recognised, however, that imperfect fitting of this could be a cause of additional errors seen for the deepest defects.

5.2 Stability

Any algorithm which extracts more information from the same data is likely to suffer more when the data has errors in it. The use of experimental data has helped to provide validation of the performance of HARBUTISM in non-ideal scenarios, dealing with both noise and systematic errors, however it is challenging to quantify the effect of such errors. The performance with different errors will be evaluated in a more controlled manner here using synthetic data.

Systematic errors are considered first. These errors are coherent between different signals causing them all to be distorted in the same way. Examples of this could be consistently mispositioning transducer locations or a change in temperature causing a change in the sound speed. To study this, the transducers will be effectively

offset; however, to avoid re-running the full FE simulation, the modelled transducer locations are kept the same, but their locations are mis-reported to the imaging algorithm, which will have an equivalent effect. The reported transducer locations are scaled by a constant factor in both in-plane dimensions, making the circular array slightly bigger or smaller. It should be noted that this is a slightly artificial scenario since, in general, the locations will be calibrated beforehand (see for example [41]) to ensure the effect of any such errors are minimised in practice. Figures 11 (a)-(e) show the results from this scaling in a range of $\pm 2\%$; for reference, a 2% error corresponds to around 20% of a wavelength for the through-transmission ray path, or 1.3 radians phase shift. It is clear that in this range the shape still remains well defined, and HARBUTISM, while inevitably being sensitive to the errors to an extent, does remain stable. When the given transducer array size is reduced, the algorithm reduces the reconstructed sound speeds to compensate, which corresponds to the background errors clearly visible in Fig. 11(a), and less so in Fig. 11(b). When the size is increased, at 1%, a slight underestimate in wall loss is apparent (corresponding to a tendency to overestimate sound speed). At 2% the HARBUTISM fitting routine has not worked because of the errors in the data preventing a better solution from being found, and the standard HARBUT reconstruction, which is the starting point of the fitting routine, is produced.

In many scenarios the effect of random noise may be significant. This can be caused by electrical noise in the acquisition system, or by any other incoherent transient effect on the system. To test these effects, noise is added to the measured data matrix prior to imaging. This is done in the frequency domain at the frequency of interest, and has normally distributed amplitude, with a standard deviation at a particular fraction of the true matrix in order to give a certain signal-to-noise ratio (SNR). The phase of each component was uniformly distributed from 0 to 2π. The results are shown in Figs. 11(f)-(i) for 6dB, 10dB, 15dB and 20dB respectively. It is clear that as the SNR increases, so does the image quality. HARBUTISM does show quite significant, large artefacts for the low SNR values, but by the 20dB point (which most modern acquisition systems can achieve easily) the image shows very little difference from the noise-free version.

5.3 Sampling

A full analysis of sampling is considered beyond the scope of this paper, however it will be briefly discussed here. Provided the wavefield is fully sampled (i.e. with less than $\lambda/2$ transducer spacing) the Born-based inversion will have sufficient data. For the array radius of 180mm and wavelength around 40mm, the minimum number of transducers therefore needed is around 57; going beyond this with over 200 transducers, as has been done in this paper, will have no effect on the resulting image. If the scattered field is used to image (rather than the total field used here) then the sampling can often be reduced further [42]. Future work will study the case when fewer transducers are used and subsampling occurs.

6 Conclusions

The majority of guided wave tomography approaches use a velocity-to-thickness mapping approach which assumes that elastic guided waves scatter from corrosion defects in the same way as acoustic waves scattering from velocity variations. This results in important inaccuracies in the reconstructions. This paper has introduced HARBUTISM, a technique which avoids this assumption, more accurately capturing the guided wave scattering when producing the thickness map. This leads to significantly improved accuracy in the reconstruction, which is partly visible as an improvement in the resolution of the image. From a resolution limit of standard velocity inversion of around 2λ, HARBUTISM has been shown to achieve at least λ and is theoretically capable of $\lambda/2$. Such resolution improvements are critical for fully capturing the complex peaks often present in real corrosion defects, which is necessary to enable the maximum wall loss to be accurately extracted. This is very important to enable the petrochemical industry assess the life of their components.

HARBUTISM was tested and compared to the velocity-to-thickness approach for a number of cases: simple axisymmetric shapes with simulated and experimental data, and on a complex simulated example taken from a laser scan of a true corrosion defect. Accuracy was improved in the majority of cases. However, for some deeper defects where wall loss was beyond 50%, modest overestimates in wall loss of around 5-10% of wall thickness were visible, which is generally not significant. It is also noted that by overestimating damage, this provides a conservative estimate of remaining life. HARBUTISM was tested with artificial sources of errors and noise, confirming itself to be robust, and produced these images in practical time-frames of less than one minute.

Finally, it should be noted that the improved scattering model is a general approach. Provided that scattering data exists to which the coefficients can be matched, it is then possible to perform an inversion to produce images.

It is therefore expected that this approach, in combination with modern high-speed simulation tools, could be applied to other areas where the inversion of complex scattering behaviour is needed.

Data

The datasets supporting this article have been uploaded as part of the supplementary material.

Competing interests

I have no competing interests.

Authors' contributions

The sole author undertook all the work in this paper.

Acknowledgements

The author would like to thank Prof. Peter Cawley for reading the manuscript.

Funding

This work was funded by EPSRC under grant number EP/M020207/1.

References

[1] D. P. Jansen and D. A. Hutchins, "Lamb wave tomography," in *Ultrasonics Symposium, 1990. Proceedings., IEEE 1990*, pp. 1017–1020, IEEE, 1990.

[2] A. Velichko and P. D. Wilcox, "Excitation and scattering of guided waves: Relationships between solutions for plates and pipes," *The Journal of the Acoustical Society of America*, vol. 125, no. 6, p. 3623, 2009.

[3] J. Pei, M. I. Yousuf, F. L. Degertekin, B. V. Honein, and B. T. Khuri-Yakub, "Lamb Wave Tomography and Its Application in Pipe Erosion/Corrosion Monitoring," *Research in Nondestructive Evaluation*, vol. 8, no. 1, pp. 189–197, 1996.

[4] W. Wright, D. Hutchins, D. Jansen, and D. Schindel, "Air-coupled Lamb wave tomography," *Ultrasonics, Ferroelectrics and Frequency Control, IEEE Transactions on*, vol. 44, no. 1, pp. 53–59, 1997.

[5] J. C. P. McKeon and M. K. Hinders, "Parallel projection and crosshole Lamb wave contact scanning tomography," *The Journal of the Acoustical Society of America*, vol. 106, no. 5, p. 2568, 1999.

[6] K. R. Leonard and M. K. Hinders, "Guided wave helical ultrasonic tomography of pipes," *The Journal of the Acoustical Society of America*, vol. 114, no. 2, pp. 767–774, 2003.

[7] K. R. Leonard and M. K. Hinders, "Lamb wave tomography of pipe-like structures," *Ultrasonics*, vol. 43, no. 7, pp. 574–583, 2005.

[8] P. Belanger, P. Cawley, and F. Simonetti, "Guided wave diffraction tomography within the born approximation," *Ultrasonics, Ferroelectrics and Frequency Control, IEEE Transactions on*, vol. 57, no. 6, pp. 1405–1418, 2010.

[9] A. Volker and J. Bloom, "Experimental Results of Guided Wave Travel Time Tomography," in *AIP Conference Proceedings*, vol. 1335, p. 215, 2011.

[10] P. Huthwaite and F. Simonetti, "High-resolution guided wave tomography," *Wave Motion*, vol. 50, no. 5, pp. 979–993, 2013.

[11] C. L. Willey, F. Simonetti, P. B. Nagy, and G. Instanes, "Guided wave tomography of pipes with high-order helical modes," *NDT & E International*, vol. 65, pp. 8–21, 2014.

[12] J. Rao, M. Ratassepp, and Z. Fan, "Guided Wave Tomography Based on Full Waveform Inversion," *IEEE Transactions on Ultrasonics, Ferroelectrics, and Frequency Control*, vol. 63, pp. 737–745, may 2016.

[13] H. Lamb, "On waves in an elastic plate," *Proceedings of the Royal Society of London. Series A*, vol. 93, no. 648, pp. 114–128, 1917.

[14] P. Huthwaite, "Evaluation of inversion approaches for guided wave thickness mapping," *Proceedings of the Royal Society A: Mathematical, Physical and Engineering Sciences*, vol. 470, pp. 20140063–20140063, apr 2014.

[15] A. C. Kak and M. Slaney, *Principles of computerized tomographic reconstruction*. New York: IEEE Press, 1998.

[16] P. Belanger and P. Cawley, "Feasibility of low frequency straight-ray guided wave tomography," *NDT & E International*, vol. 42, no. 2, pp. 113–119, 2009.

[17] P. Huthwaite and F. Simonetti, "High-resolution imaging without iteration: a fast and robust method for breast ultrasound tomography.," *The Journal of the Acoustical Society of America*, vol. 130, p. 1721, sep 2011.

[18] P. Huthwaite, "Improving accuracy through density correction in guided wave tomography," *Proceedings of the Royal Society A: Mathematical, Physical and Engineering Sciences*, vol. 472, no. 2186, 2016.

[19] C. Vemula and A. Norris, "Flexural wave propagation and scattering on thin plates using Mindlin theory," *Wave Motion*, vol. 26, pp. 1–12, aug 1997.

[20] A. H. Rohde, M. Veidt, L. R. F. Rose, and J. Homer, "A computer simulation study of imaging flexural inhomogeneities using plate-wave diffraction tomography.," *Ultrasonics*, vol. 48, pp. 6–15, mar 2008.

[21] L. R. F. Rose and C. H. Wang, "Mindlin plate theory for damage detection: imaging of flexural inhomogeneities.," *The Journal of the Acoustical Society of America*, vol. 127, pp. 754–63, feb 2010.

[22] L. Moreau, A. Hunter, A. Velichko, and P. Wilcox, "3-D reconstruction of sub-wavelength scatterers from the measurement of scattered fields in elastic waveguides," *IEEE Transactions on Ultrasonics, Ferroelectrics, and Frequency Control*, vol. 61, pp. 1864–1879, nov 2014.

[23] L. Bourgeois and E. Lunéville, "The linear sampling method in a waveguide: a modal formulation," *Inverse Problems*, vol. 24, p. 015018, feb 2008.

[24] S. Rodriguez, M. Deschamps, M. Castaings, and E. Ducasse, "Guided wave topological imaging of isotropic plates," in *Ultrasonics*, vol. 54, pp. 1880–1890, 2014.

[25] P. M. Morse and K. U. Ingard, *Theoretical Acoustics*. New York, London: McGraw-Hill Book Company, 1968.

[26] T. Grahn, "Lamb wave scattering from a circular partly through-thickness hole in a plate," *Wave Motion*, vol. 37, no. 1, pp. 63–80, 2003.

[27] F. Cegla, A. Rohde, and M. Veidt, "Analytical prediction and experimental measurement for mode conversion and scattering of plate waves at non-symmetric circular blind holes in isotropic plates," *Wave Motion*, vol. 45, no. 3, pp. 162–177, 2008.

[28] P. Huthwaite, "Accelerated finite element elastodynamic simulations using the GPU," *Journal of Computational Physics*, vol. 257, no. A, pp. 687–707, 2014.

[29] B. Pavlakovic, M. Lowe, D. Alleyne, and P. Cawley, "Disperse: a general purpose program for creating dispersion curves," *Review of progress in quantitative nondestructive evaluation*, vol. 16, pp. 185–192, 1997.

[30] E. Chan, L. F. Rose, and C. H. Wang, "A comparison and extensions of algorithms for quantitative imaging of laminar damage in plates. II. Non-monopole scattering and noise tolerance," *Wave Motion*, vol. 66, pp. 220–237, 2016.

[31] J. Su, L. R. F. Rose, M. Veidt, and C. H. Wang, "Use of the mode-converted scattered Lamb waves for baseline-free imaging of structural damage," in *8th Australasian Congress on Applied Mechanics*, vol. Part B, pp. 389–400, Engineers Australia, 2014.

[32] M. Born and E. Wolf, *Principles of Optics*. Cambridge: Cambridge University Press, 1999.

[33] A. J. Devaney, "A filtered backprojection algorithm for diffraction tomography," *Ultrasonic Imaging*, vol. 4, pp. 336–350, oct 1982.

[34] P. Huthwaite, *Quantitative Imaging with Mechanical Waves*. PhD thesis, Imperial College London, 2012.

[35] B. W. Drinkwater and P. D. Wilcox, "Ultrasonic arrays for non-destructive evaluation: A review," *NDT & E International*, vol. 39, no. 7, pp. 525–541, 2006.

[36] L. R. F. Rose, E. Chan, and C. H. Wang, "A comparison and extensions of algorithms for quantitative imaging of laminar damage in plates. {I}. Point spread functions and near field imaging," *Wave Motion*, vol. 58, pp. 222–243, 2015.

[37] F. Simonetti and L. Huang, "From beamforming to diffraction tomography," *Journal of Applied Physics*, vol. 103, p. 103110, 2008.

[38] P. Huthwaite, F. Simonetti, and N. Duric, "Combining time of flight and diffraction tomography for high resolution breast imaging: initial in vivo results (L).," *The Journal of the Acoustical Society of America*, vol. 132, p. 1249, sep 2012.

[39] J. A. Sethian, "Fast marching methods," *SIAM review*, pp. 199–235, 1999.

[40] R. J. Lavarello and M. L. Oelze, "Density imaging using inverse scattering," *The Journal of the Acoustical Society of America*, vol. 125, no. 2, pp. 793–802, 2009.

[41] M. Seher, P. Huthwaite, and M. Lowe, "Experimental Studies of the Inspection of Areas with Restricted Access Using A0 Lamb Wave Tomography," *IEEE Transactions on Ultrasonics, Ferroelectrics, and Frequency Control*, pp. 1–1, 2016.

[42] F. Simonetti, L. Huang, and N. Duric, "On the spatial sampling of wave fields with circular ring apertures," *Journal of Applied Physics*, vol. 101, no. 8, p. 083103, 2007.